

## General Disclaimer

### One or more of the Following Statements may affect this Document

- This document has been reproduced from the best copy furnished by the organizational source. It is being released in the interest of making available as much information as possible.
- This document may contain data, which exceeds the sheet parameters. It was furnished in this condition by the organizational source and is the best copy available.
- This document may contain tone-on-tone or color graphs, charts and/or pictures, which have been reproduced in black and white.
- This document is paginated as submitted by the original source.
- Portions of this document are not fully legible due to the historical nature of some of the material. However, it is the best reproduction available from the original submission.

*DRA*

**THE SOLAR FLARE IRON LINE TO CONTINUUM RATIO**

**AND**

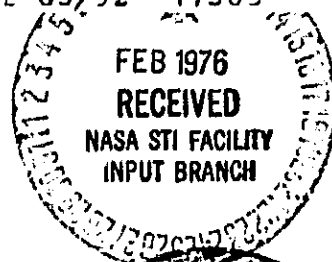
**THE CORONAL ABUNDANCES OF IRON AND HELIUM**

(NASA-CR-146358) THE SOLAR FLARE IRON LINE TO CONTINUUM RATIO AND THE CORONAL ABUNDANCES OF IRON AND HELIUM (Aerospace Corp., El Segundo, Calif.) 37 p HC \$4.00

N76-17011

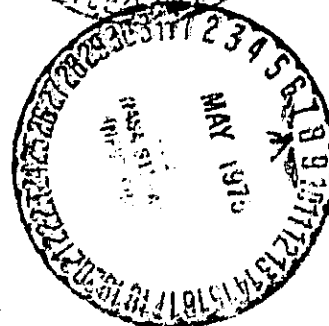
Unclas  
CSCI G3B G3/92 17365

Prepared by  
**D. L. McKenzie**  
Space Physics Laboratory



29 April 1975

Laboratory Operations  
**THE AEROSPACE CORPORATION**  
El Segundo, California



Prepared for  
National Aeronautics and Space Administration  
Washington, D. C.

Contract No. NASW-2614



**THE AEROSPACE CORPORATION**

THE SOLAR FLARE IRON LINE TO CONTINUUM RATIO  
AND  
THE CORONAL ABUNDANCES OF IRON AND HELIUM

Prepared by  
D. L. McKenzie  
Space Physics Laboratory

29 April 1975

Laboratory Operations  
THE AEROSPACE CORPORATION  
El Segundo, California

Prepared for  
National Aeronautics and Space Administration  
Washington, D. C.

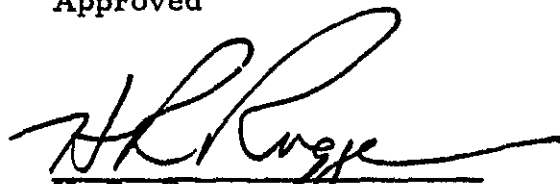
Contract No. NASW-2614


THE SOLAR FLARE IRON LINE TO CONTINUUM RATIO  
AND THE CORONAL ABUNDANCES OF IRON AND HELIUM

Prepared

  
D. L. McKenzie  
Space Physics Laboratory

Approved

  
H. R. Ruge  
Space Physics Laboratory

  
G. A. Paulikas  
Space Physics Laboratory

PRECEDING PAGE BLANK NOT FILMED

## CONTENTS

ABSTRACT . . . . .	1
1. Introduction . . . . .	2
2. Instrumentation . . . . .	4
3. Calculation of Iron Line Emission . . . . .	8
4. Data Analysis . . . . .	11
5. Results . . . . .	17
6. Discussion . . . . .	22
FIGURES . . . . .	24
REFERENCES . . . . .	33

PRECEDING PAGE BLANK NOT FILMED

## ABSTRACT

The purpose of this investigation was to use narrow band Ross filter measurements of the Fe XXV line flux around 0.185 nm wavelength and simultaneous broad band measurements during a solar flare to determine the relationship between the solar coronal abundances of iron and helium. A second purpose was to determine the Fe XXV ion population as a function of time during a flare. Broad band measurements from the UCSD proportional counter and Ross filter measurements from the Goddard Space Flight Center instrument, both on OSO-7, were taken of a flare at UT 0300 on 27 October, 1972. The UCSD measurements gave the temperature and emission measure as a function of time and allowed line and continuum to be separated in the Goddard measurements. The data were analyzed under two separate assumptions: that the electron density was high enough that a single temperature could characterize the continuum spectrum and the ionization equilibrium, and that the electron density was low so that the ion populations trailed the electron temperature in time. Using the imaging property of the Goddard experiment, we found that the density was at least  $5 \times 10^9$ , and that the high density assumption was valid. Fitting the observed line strength to the measured temperature and emission measure we found the iron abundance to be  $1.1 \times 10^{-5}$  for a helium abundance of 0.2, relative to hydrogen. This result can be made consistent with previously determined iron abundances around  $2 \times 10^{-5}$  but not with much higher values. An absolute determination of the helium abundance by this method awaits the analysis of many good iron spectra.

## 1. Introduction

The purpose of this investigation is to measure the iron line to continuum ratio in the wavelength range around 0.185 nm. In the past the line emission has been measured using crystal spectrometers (Neupert, et al., 1967), while continuum measurements have been made using broad band instruments such as proportional counters (McKenzie, et al., 1973). Because crystal spectrometers have low efficiency, and proportional counters experience saturation and pulse pileup difficulties at high counting rates, the line to the continuum ratio has not been measured previously. This investigation uses data from the Goddard Space Flight Center iron line Ross balanced filter pair and the University of California at San Diego proportional counter, both on OSO-7. Once the line to continuum ratio has been determined, we use theoretical calculations of the line strength to estimate the relative coronal abundances of iron and helium and to examine the time dependent population of the helium-like ion, Fe XXV.

Table I presents the thresholds for the channels of the UCSD proportional counter. These values are discussed in a later section. The iron line emission falls primarily in channel 4. We therefore fit the data in channels 3 and 5-8 to a model spectrum to obtain values of the flare electron temperature,  $T$ , and emission measure (EM), defined as:

$$EM = \int_V n_e^2 dV, \quad (1.1)$$

where  $n_e$  is the flare electron density, and the integral is over the flare volume. These determinations allow the continuum at 0.185 nm to be estimated.

The GSFC Ross balanced filter pair measures the flux in a narrow, well-defined energy range. Using the UCSD continuum determination we separate the line flux from the continuum within the Ross filter band pass. This gives us the line to continuum ratio. Using theoretical calculations of the line and continuum fluxes we are then able to estimate the relationship between the solar iron and helium abundances. This is possible because the contribution of helium to the continuum flux is second in importance only to that of hydrogen. Again using theoretical models, the population of Fe XXV as a function of time is estimated from the line flux.

Table I

## UCSD Energy Channel Thresholds

<u>Channel Number</u>	<u>Prelaunch Threshold (nm)</u>	<u>Threshold at <math>10^4</math> c/sec (nm)</u>	<u>Threshold at <math>2 \times 10^4</math> c/sec (nm)</u>
1	0.65	0.62	0.59
2	0.52	0.49	0.47
3	0.34	0.32	0.30
4	0.24	0.23	0.22
5	0.19	0.17	0.16
6	0.155	0.148	0.141
7	0.133	0.127	0.121
8	0.117	0.111	0.106



## 2. Instrumentation

Figure 1, a plot of the mass absorption coefficients of iron and manganese as a function of wavelength may be used in discussing the operational principle of the Ross balanced filters. The mass absorption coefficient for each material jumps dramatically at its K shell absorption edge wavelength. The transmission of, for example, a thin iron filter is given by

$$T_{Fe} = e^{-\mu_{Fe} X_{Fe}}, \quad (2.1)$$

where  $\mu_{Fe}$  is the mass absorption coefficient in  $\text{cm}^2/\text{g}$  and  $X$  is the filter thickness in  $\text{gm}/\text{cm}^2$ . According to Figure 1, there exist values of  $X_{Fe}$  and  $X_{Mn}$  such that the transmissions of iron and manganese filters are equal except in the region between the two elements' absorption edges (0.174 - 0.190 nm). A Ross filter system consists of a pair of such balanced filters in front of identical detectors. The difference in the counting rates of the two counters is then a measure of the X-ray flux in the narrow passband, 0.174 - 0.190 nm. In addition to the narrow band, the Ross filter system has a second advantage. The effective detector passband is precisely set by the filter absorption edge energies, and is therefore not subject to electronics drift uncertainties. The electronic threshold needs only to be set at a low enough energy that all detected photons of wavelength shorter than 0.19 nm will be counted.

The Goddard Ross filter system consists of the balanced filters with their identical proportional counters located in back of a multigrid collimator. The properties of the system were measured before launch or are easily calculable. The collimator is continuously rastered over a 5 arc minute x 5 arc minute region in the mode employed for this measurement. Data are read out 368 times during the raster which takes 61.44 seconds to complete.

The system response may be computed as the product of the efficiencies of the various components:

$$R = A \epsilon_c \epsilon_F T_c t_{eff} \quad \text{cm}^2\text{-sec}, \quad (2.2)$$

where  $A$  is the window area of one counter ( $2.2 \text{ cm}^2$ , taking into account a preflight adjustment to bring the system into balance),  $\epsilon_c$  is the calculated counter efficiency,  $\epsilon_F$  is the filter transmission difference in the passband

(0.62),  $T_c$  is the collimator transmission, and  $t_{\text{eff}}$  is the effective average exposure time for each point in the raster. The counter efficiency is the absorption of a 1.05 cm path length of 90% xenon multiplied by the transmission of the 0.012 gm/cm<sup>2</sup> beryllium window. This comes out to be 0.912. The on-axis collimator transmission is 0.12, and the collimator field of view is 15.5 arc seconds, FWHM (Sterk, et al., 1972). Since the raster line spacing is 20 arc seconds and the collimator FWHM is 15.5 arc seconds, the collimator response must be multiplied by a factor to account for the fact that all points are not swept over by the same effective area. Assuming a triangular response, which characterizes a multigridded collimator of the type used, this factor is 0.775. During a raster, each point is observed while the collimator sweeps over 31 arc seconds, with an average of one-half the on-axis transmission during this period (again assuming a triangular response). Thus

$$t_{\text{eff}} = \frac{1}{2} (31 \text{ arc sec/scan rate}) . \quad (2.3)$$

The scan rate is 78.125 arc sec/sec. Then, equation (2.2) gives  $R = .0229 \text{ cm}^2\text{-sec}$ . The conversion factor from raster counts to flux is  $R^{-1} = 43.6 \text{ photons/}(\text{cm}^2\text{-sec})$  per raster count.

The UCSD detector with which we are concerned is a proportional counter of 2.54 cm diameter filled with a one-atmosphere 90% Xe, 10% CO<sub>2</sub> gas mixture. The counter has a 0.115 gm/cm<sup>2</sup> beryllium window of area 0.32 cm<sup>2</sup>. The instrument gain and resolution were measured prior to launch. Its behavior at high counting rates was also observed in the laboratory. The wavelength threshold of each channel is given in Table I. In addition to the prelaunch nominal values we have noted the effective values at counting rates of  $10^4$  and  $2 \times 10^4 \text{ sec}^{-1}$  at the time of the observations discussed here, in the fall of 1972. These values will be discussed below. With the exception of channel 4, channels 3-8 are dominated by continuum, as opposed to line, flux.

The response of the UCSD detector to model thermal X-ray spectra was determined for temperatures in the range  $1\text{-}3 \times 10^7 \text{ K}$ . Model spectra which included the continuum processes of bremsstrahlung, radiative recombination, and two-photon decay from metastable levels in hydrogen- and helium-like ions were folded through the instrument efficiency and resolution functions. It is

convenient to use these data in the form of ratios of channel N counts to channel 3 counts, with  $N > 3$ . Channels 1 and 2 have important line contributions and efficiencies that change rapidly as a function of energy, so the data in these channels were not used in this analysis program. Sets of curves of the ratios were generated for counter gains equal to the nominal value divided by a parameter, k. Figure 2 shows the set for  $k = 1.06$ .

For the analysis undertaken here it was necessary to include the instrument response to iron line emission around 0.185 nm. Furthermore the data included samples with detector integral counting rates in the range  $1-2 \times 10^4 \text{ sec}^{-1}$ . In prelaunch measurements, using a  $\text{Fe}^{55}$  radioactive source (0.21 nm), we observed a gain decrease of about 5% at a total counting rate of  $2 \times 10^4 \text{ sec}^{-1}$ . Culhane, et al. (1967) observed a similar decrease in their OSO-4 instrument. The effect is attributed to a build up of positive ions in the counter gas. The resolution is not impaired, and we use the prelaunch values for our analysis. Also, since the instrument pulse pair resolving time is 3.2  $\mu\text{sec}$ , at a rate of  $2 \times 10^4 \text{ sec}^{-1}$  approximately 6.2% of the pulses will "pile-up," adding their amplitudes to those of preceding pulses.

To take into account the effects described in the previous paragraph, a Monte Carlo program was written. The low counting rate model spectra, broadened and folded through the instrument efficiency were used as input. The pulse shape and the peak detecting operation of the electronics were properly taken into account. The iron line was broadened according to the instrument resolution and was included in the input spectrum. The output spectrum was displayed in energy bins  $3.2 \times 10^{-17}$  joules (0.2 keV) wide. These data were gathered into energy channels assuming a gain shift by a small factor, k, as described above, with an additional 5% decrease at  $2 \times 10^4 \text{ sec}^{-1}$ . Comparing with actual flare spectra resulted in good fits for  $k = 1.05$ . A five percent gain deterioration after more than a year's continuous operation is not unreasonable.

Figure 3 shows the Monte Carlo program results for an integral counting rate of  $2 \times 10^4 \text{ sec}^{-1}$ , including a line counting rate of  $1 \times 10^3 \text{ sec}^{-1}$ . Other runs varied both counting rates. A few remarks comparing Figure 2 and Figure 3 would be appropriate. In Figure 3, the channel 4 curve is higher than that for Figure 2, reflecting the inclusion of line emission. For the other channels, Figure 3 shows enhanced counting rates, particularly at low temperatures

and high energies, where the thermal spectrum is steepest. This indicates that pileup is the major effect, since a decrease in gain would lower the counting rates in the higher channels. The relatively small number of pileup events form a significant fraction of the counts where the "real" counting rate is small. The error bars in Figure 3 are  $\pm 1 \sigma$ .

### 3. Calculation of Iron Line Emission

The iron line flux around 0.185 nm consists of the  $1s^2 1S - 1s2p^1P$  resonance line, the forbidden  $1s^2 1S - 1s2p^3S$  line, the  $1s^2 1S - 1s2p^3P$  intercombination lines, all from Fe XXV, and satellite lines from Fe XXIV emitted following inner shell excitation or dielectronic recombination.

The resonance line emission from a coronal plasma is discussed by Walker (1972). For the  $1s^2 1S - 1s2p^1P$  transition (hereinafter called the "resonance" line) of Fe XXV, the energy flux at the Earth is

$$\phi_R = (EM) A_{Fe} a_{24} 5.01 \times 10^{-44} (z^{2\bar{n}})_{Ly\alpha} \frac{f_R}{f_{Ly\alpha}} B_R \frac{e^{-E_R/kT}}{\sqrt{T}} \quad (3.1)$$

(erg-cm<sup>-2</sup>-sec<sup>-1</sup>).

In equation (3.1):

- EM = emission measure,
- $A_{Fe}$  = iron abundance,
- $a_{24}$  = fractional population of 24 times ionized Fe XXV (from Jordan, 1970),
- $z$  = the ionic charge,
- $(z^{2\bar{n}})_{Ly\alpha}$  the temperature averaged collision strength for the Lyman alpha transition in Fe XXVI,
- $f_R$  = the resonance line oscillator strength,
- $f_{Ly\alpha}$  = the Lyman alpha oscillator strength,
- $B_R$  = the branching ratio of the resonance line,
- $E_R$  = the excitation energy of the resonance line,
- $T$  = the electron temperature (K), and
- $k$  = Boltzmann's constant.

Note that equation (3.1) calculates the resonance line collision strength from that for the Lyman alpha line. If the electron density is low the ion populations may be characterized by a temperature,  $T_z$ , which differs from  $T$ . In such cases, equation (3.1) may be used with  $a_{24}$  equal to  $a_{24}(T_z)$ .

Following dielectronic recombination the lithium-like ion, Fe XXIV, may be in a state  $1s2p n\ell$ . If it undergoes the transition,  $1s^2 n\ell - 1s2pn\ell$  rather than autoionizing, the emitted photon has a wavelength nearly the same as that of

the resonance line. For  $n > 3$ , the "satellite lines" are generally unresolvable from the resonance line. The unresolved dielectronic recombination flux may be related to the resonance line flux by

$$\phi_{UD} = \alpha \phi_R, \quad (3.2)$$

where

$$\alpha = \frac{5.375 \times 10^6}{(z^2 \bar{\Omega})_{Ly\alpha} T} \quad (3.3)$$

for Fe XXV. Since  $(z^2 \bar{\Omega})_{Ly\alpha} = 1.6$ , the unresolved dielectronic recombination satellite lines make up 16-35% of the measured resonance line flux. Equation (3.3), based upon an extrapolation of the work of Shore (1969) to high Z, probably overestimates  $\alpha$ . Walker (personal communication) has recalculated  $\alpha$  to arrive at (for Fe XXV)

$$\alpha = \frac{2.19 \times 10^6}{(z^2 \bar{\Omega})_{Ly\alpha} T}. \quad (3.4)$$

We performed the analysis using equation (3.3), however. The resonance line flux one would measure,  $\phi_s$ , is the sum of  $\phi_R$  and  $\phi_{UD}$ .

The forbidden and intercombination line emission has been discussed by Gabriel and Jordan (1969, 1973) and Blumenthal, et al. (1972). The sum of these lines is related to the resonance line by an experimentally determined parameter, G:

$$\phi_{I+F} = G \phi_s. \quad (3.4)$$

Equation (3.4) uses  $\phi_s$  since G is an experimental parameter. G has been determined for low Z elements. Rugge and Walker (1971) found  $G = 1.1$ . We use this value in the absence of a measurement for iron.

Gabriel (1972) and Bhalla et al., (1975) have calculated the resolved satellite line fluxes ( $n = 2$ ). For an individual line excited by dielectronic recombination,

$$\frac{\phi_D}{\phi_s} \propto \frac{1}{(1+\alpha)} \frac{E_R}{T} e^{-(E_R - E_D)/kT} \times \frac{g_s A_r A_a}{(A_a + \sum A_r)} \quad (3.5)$$

Here  $E_R$  and  $E_D$  are the resonance and satellite line energies,  $g_s$  is the satellite level statistical weight, and  $A_r$  and  $A_a$  are the radiative decay and autoionization transition probabilities.

Gabriel rewrites (3.5) as

$$\left(\frac{\phi_D}{\phi_s}\right)_T = F_D(T) \cdot \left(\frac{\phi_D}{\phi_s}\right)_{T_m} \quad (3.6)$$

separating out the temperature dependence. The second factor is the ratio evaluated at  $T_m$ , the temperature at which resonance line emission is a maximum. For our broad band measurements we sum (3.6) over the satellite lines, all of which lie in the Ross filter pass band. According to Bhalla et al. (1975),

$$\phi_D(T) = \phi_s(T) \left[ 0.2963 F_D(T) \right] \quad (3.7)$$

$F_D(T)$  is tabulated by Bhalla et al. and shown in Figure 4.

Because the inner shell excitation line strengths depend on the relative populations of Fe XXIV and Fe XXV, they are related to the resonance line strength through  $T_z$ . According to Gabriel,

$$\frac{\phi_I}{\phi_R} = \frac{a_{23}}{a_{24}} \frac{1}{1+\alpha} \times \beta \frac{f_I}{f_R} \frac{A_r}{A_a + \sum A_r} \quad (3.8)$$

where  $\beta$  is the probability that the Fe XXIV ion is in the proper initial state to be excited and emit the satellite line in question and the  $f$ 's are effective oscillator strengths. As in (3.7) we write

$$\phi_I(T, T_z) = \phi_s(T, T_z) \left[ 0.0808 F_I(T_z) \right] \quad (3.9)$$

$F_I(T_z)$  is plotted in Figure 4.

#### 4. Data Analysis

Three events occurring on 27 October, 29 October, and 3 November, 1972, were selected by Dr. Roger J. Thomas of Goddard for possible analysis. All three events occurred in McMath Plage Region 12094. The 3 November burst had UCSD counting rates of  $5 \times 10^4$  -- too high for reliable spectral analysis. The 27 October event had low counting rates and probably occurred partially outside the range of the OSO small raster. Therefore only the event occurring at U1 0259-0323 on 29 October was suitable for analysis. The event had just started at the OSO night-day transition, so the analysis covers the flare peak and decay phases.

The Goddard data is output as one raster every 61.44 seconds. C, the difference in the total counts behind the two filters, is printed out. In addition, at each of the 368 readout points in the raster is recorded a "-2", a "0" or an even positive integer. If the manganese filter counts exceed the iron filter counts at "-2" is recorded. The even positive integers, n, represent a difference of n or n+1 counts with the iron filter count higher. Outside flaring regions, recordings higher than +2 are rare. Therefore readings of n = 4 or greater were regarded as real and counted as n+1/2 counts, if they occurred in the flaring region. Readings of 2 were counted as 2 counts in the flaring region. Readings of 0 and -2 were not counted. The UCSD counting rate varied slowly with time, and the Goddard rate was assumed to be constant during that part of the raster that covered the flaring region.

To find the Goddard flux we first compute the sum of the individual counts  $c_i$  as outlined in the previous paragraph. We then need to subtract out background at the  $n_f$  flare points in the raster. The total number of background counts at  $368-n_f$  points is

$$B = C - \sum_{i=1}^{n_f} c_i, \quad (4.1)$$

so that the background at the  $n_f$  points is

$$B_f = \left( C - \sum_{i=1}^{n_f} c_i \right) \frac{n_f}{368-n_f}. \quad (4.2)$$

Then the total number of flare counts is



$$C_f = \sum_{i=1}^{n_f} c_i - B_f = r \sum_{i=1}^{n_f} c_i - \frac{r-1}{r} C \quad (4.3)$$

where

$$r = 1 + \frac{n_f}{368 - n_f} \quad (4.4)$$

From Section 2, the GSFC flux,  $\Phi_G$ , is given by

$$\Phi_G = 43.6 C_f \quad (4.5)$$

The fluxes are plotted in Figure 5.

From the given data alone, the probable error in  $\Phi_G$  cannot be calculated. However, the data measured consists of both line and continuum. The UCSD data, mostly continuum, varies smoothly with time. The ionization time for Fe XXV is given by (Cox and Tucker, 1970)

$$t_I = \frac{2.43 \times 10^{-5}}{N_9 \sqrt{T_7}} \frac{I_{eV}^2 e^{I/kT}}{\xi F(Z, z)} \quad (4.6)$$

Here  $T_7$  is the temperature times  $10^{-7}$  K,  $N_9$  is the electron density times  $10^{-9} \text{ cm}^{-3}$ ,  $I_{eV}$  is (ground state ionization potential /  $1.6 \times 10^{-19}$  joules),  $\xi = 1$ , and  $F(Z, z) = 1.8$ . Thus  $t_I \sim 131/N_9$  for  $T = 2 \times 10^7$  K. Similarly the recombination time is given by

$$t_R = 10^4 T_7^{1/2} / Z N_9 \quad (4.7)$$

where  $Z = 26$ . At  $2 \times 10^7$  K,  $t_R = 544/N_9$ . Thus, since the continuum flux and temperature vary smoothly, the total flux in the Ross filter pass band should be a smooth function of time. We therefore made a least squares linear fit to  $\Phi_G = mt + b$ , with  $t$  measured in seconds from 0300 UT, and found  $m = -3.865$  and  $b = 8093$ . This curve is shown in Figure 5. The rms deviation of the data from this curve,  $1384 \text{ photon-cm}^{-2}\text{-sec}^{-1}$ , is an estimate of the error in  $\Phi_G$ .

The UCSD measurements were used to separate the line and continuum components of  $\Phi_G$ . As noted above, UCSD channels 3 and 5-8 are strongly dominated by continuum. The Monte Carlo program was used to find the best fit temperature and emission measure as described in Section 2. Using these parameters and the Aerospace model X-ray spectrum computer program, the continuum flux in the 0.174 - 0.190 Å range was computed and subtracted from  $\Phi_G$  to obtain the line flux. Input line counting rates of five and ten percent of the total UCSD integral rate were used. Comparison of the resulting line fluxes with those input to the UCSD program for consistency indicated that the lower line fluxes were more accurate. Since the continuum obtained in this way is essentially an interpolation of the UCSD data, we estimate the continuum subtraction contributes at worst an error of 20% of the line flux. Table II shows the results of this computation, assuming a helium abundance of 0.20 to calculate the emission measure, and taking  $\Phi_G$  from the fit in Figure 5. The temperature was determined as an average of the values obtained for channels 5-8 using plots such as Figure 3, assuming an isothermal plasma. The errors are the rms deviations from the quoted values.

If a low density plasma is assumed, an estimate of the Fe XXV population,  $a_{24}(T_z)$ , and of  $T_z$  may be obtained from the data. Values for  $A_{Fe}$  and  $A_{He}$  must be assumed. Combining equations (3.1), (3.2), (3.4), (3.7), and (3.9) gives for the total line flux,

$$\Phi_T(T, T_z) = \frac{\Phi_s(T)}{E_R} \frac{a_{24}(T_z)}{a_{24}(T)} \left[ 1 + G + .2963 F_D(T) + .0808 F_I(T_z) \right] \quad (4.8)$$

photon-cm<sup>-2</sup>-sec<sup>-1</sup>

In equation (4.8), the factor  $E_R^{-1}$  converts from energy to photon flux under the approximation that all lines included have the same wavelength. The ratio of the ion populations is introduced since the applicable one is  $a_{24}(T_z)$  and  $\Phi_s(T)$  contains the factor  $a_{24}(T)$ . Since the inner shell term is usually small, we begin by setting the line flux from Table II,  $\Phi_L$ , equal to the remainder of equation (4.8):

$$\Phi_L = \frac{\Phi_s(T)}{E_R} \frac{a_{24}(T_z)}{a_{24}(T)} \left[ 1 + G + .2963 F_D(T) \right] \quad (4.9)$$

Table II

Time	$\Phi_G$ ( $\text{cm}^{-2}\text{sec}^{-1}$ )	$\Phi_c$ ( $\text{cm}^{-2}\text{sec}^{-1}$ )	$\Phi_L$ ( $\text{cm}^{-2}\text{sec}^{-1}$ )	T ( $10^6\text{K}$ )	EM ( $10^{48}\text{cm}^{-3}$ )
0301:45	7687	3279	4403	$21.2 \pm 0.9$	1.31
0302:53	7424	4543	2881	$22.2 \pm 1.0$	1.58
0303:48	7204	4960	2244	$22.2 \pm 0.7$	1.67
0304:50	6972	4805	2167	$21.7 \pm 1.1$	1.79
0305:57	6713	4394	2319	$20.0 \pm 0.8$	2.14
0306:58	6477	4120	2357	$19.1 \pm 0.6$	2.35
0308:00	6238	3750	2488	$17.9 \pm 0.3$	2.64
0308:56	6021	3525	2496	$17.4 \pm 0.4$	2.87
0309:57	5786	3158	2628	$16.5 \pm 0.3$	3.18
0311:04	5526	2553	2973	$15.1 \pm 0.4$	3.79
0312:06	5287	2219	3068	$14.4 \pm 0.9$	4.10
0313:01	5074	2073	3001	$14.1 \pm 0.9$	4.26
0314:09	4812	1775	3037	$13.3 \pm 0.8$	4.86
0315:04	4599	1778	2821	$13.5 \pm 0.9$	4.50
0316:11	4340	1378	2962	$12.4 \pm 1.1$	5.47
0317:13	4100	1233	2867	$12.2 \pm 1.0$	5.40
0318:08	3888	1106	2782	$11.9 \pm 0.9$	5.60
0319:10	3648	923	2725	$11.4 \pm 0.5$	5.96

With assumed values of  $A_{\text{He}}$  and  $A_{\text{Fe}}$  and measured  $T$  and  $EM$ , equation (4.9) is solved for  $a_{24}(T_z)/a_{24}(T)$ . Since  $a_{24}(T)$  is known,  $a_{24}(T_z)$  and, hence,  $T_z$  may be calculated. This value may then be used to find the inner shell excitation contribution to the flux and equation (4.8) may be iterated to improve the estimates of  $a_{24}(T_z)$  and  $T_z$ .

Table III summarizes the results of the calculation in the preceding paragraph for  $A_{\text{Fe}} = 2.0 \times 10^{-5}$  and  $A_{\text{He}} = 0.2$ . For lower  $A_{\text{He}}$  the emission measure increases as Figure 6, which plots the calculated continuum for  $A_{\text{He}} = 0.2$  and  $A_{\text{He}} = 0.15$  relative to that for  $A_{\text{He}} = 0.07$ , illustrates. For higher  $A_{\text{Fe}}$ ,  $a_{24}(T_z)$  is, of course, lower, since the line flux is proportional to  $A_{\text{Fe}} \times a_{24}(T_z)$ .

Table III also records the product  $T \cdot EM$ . Assuming a constant flare density as a function of time,  $T \cdot EM$  is a measure of the flare energy content since the thermal energy,  $E_T$ , is

$$E_T = \frac{3}{2} (n_e + \sum_I n_I) V k T, \quad (4.10)$$

where  $V$  is the volume and the sum is over all ions present in the plasma. Since

$$\sum_I n_I \approx n_H (1 + A_{\text{He}}), \quad (4.11)$$

and at coronal temperatures

$$n_e \approx n_H (1 + 2A_{\text{He}}), \quad (4.12)$$

we have

$$E_T \approx \frac{3}{2} n_e V k T \left( 1 + \frac{1 + A_{\text{He}}}{1 + 2A_{\text{He}}} \right). \quad (4.13)$$

Finally we rewrite (4.13):

$$E_T \approx \frac{3}{2} \frac{EM}{n_e} k T \left( 1 + \frac{1 + A_{\text{He}}}{1 + 2A_{\text{He}}} \right). \quad (4.14)$$

Table III indicates that the flare energy content continues to rise even as the flare cools. A similar result was reported by McKenzie, et al. (1973). Numerically, the peak energy is  $2.6 \times 10^{40} / n_e$  ergs.

Table III

Time	T ( $10^6$ K)	EM ( $10^{49}$ cm $^{-3}$ )	EM · T ( $10^{55}$ cm $^{-3}$ K)	$a_{24}(T)$	$a_{24}(T_z)$	T <sub>z</sub> ( $10^6$ K)
0301:45	21.2	1.31	2.78	.693	.501	17.9
0302:53	22.2	1.58	3.51	.726	.230	14.7
0303:48	22.2	1.67	3.71	.726	.176	14.0
0304:50	21.7	1.79	3.88	.713	.150	13.6
0305:57	20.0	2.14	4.28	.646	.168	13.9
0306:58	19.1	2.35	4.49	.594	.176	14.0
0308:00	17.9	2.64	4.73	.503	.213	14.4
0308:56	17.4	2.87	4.99	.455	.200	14.3
0309:57	16.5	3.13	5.25	.394	.230	14.7
0311:04	15.1	3.79	5.72	.268	.282	15.2
0312:06	14.4	4.10	5.90	.209	.314	15.5
0313:01	14.1	4.26	6.01	.186	.322	15.6
0314:09	13.3	4.86	6.46	.125	.336	15.7
0315:04	13.5	4.50	6.08	.140	.318	15.5
0316:11	12.4	5.47	6.78	.076	.373	16.0
0317:13	12.2	5.40	6.59	.068	.394	16.5
0318:08	11.9	5.60	6.66	.055	.426	17.1
0319:10	11.4	5.96	6.79	.036	.405	16.7

REPRODUCIBILITY OF THE  
ORIGINAL PAGE IS POOR

## 5. Results

The data were analyzed under two assumptions. First the electron density was assumed to be low enough that  $T_z$  could differ from  $T$ . Second, an estimate of  $A_{Fe}$  was made assuming  $T_z = T$ .

Table III in Section 4 presents some of the results obtained under the low density assumption. The time development of  $a_{24}(T_z)$  does not occur as one would expect. For times at which  $T$  exceeds  $T_z$  the plasma should be ionizing; that is  $T_z$  should be increasing. Kafatos and Tucker (1972) show some calculated ion population curves for hypothetical X-ray flares. Because of the large probable error in  $\phi_G$ , the data in Table III may not be inconsistent with the expected theoretical flare decay.

A second approach was taken to comparing theoretical low density calculations to the experimental data. For any ion, the ionization balance equation is (Kafatos and Tucker, 1972)

$$\frac{da_z}{dt} = n_e (\alpha_{z+1} a_{z+1} - \alpha_z a_z + Q_{z-1} a_{z-1} - Q_z a_z) \quad (5.1)$$

In equation 5.1,  $a_z$  is the fractional population of the ion with charge  $z$ ,  $\alpha_z$  is the total recombination coefficient for the process  $z \rightarrow z-1$ , and  $Q_z$  is the ionization coefficient for  $z \rightarrow z+1$ . Iron near or in a solar flare may be in any state from  $\sim$  Fe XVI to Fe XXVI so that to obtain  $a_z$  is a function of time a large number of coupled equations must be solved. We have made a number of simplifying assumptions in treating equations (5.1). We assumed that only three stages of ionization are important: Fe XXIII, Fe XXIV, and Fe XXV. All iron in states below Fe XXIII was added to that in Fe XXIII. This is not too bad an approximation since the ionization time for Fe XXII is only  $\sim 50/N_9$  seconds. The approximation slightly increases the Fe XXV ionization rate. The second approximation was to ignore recombination from Fe XXVI to Fe XXV. At the temperatures,  $T$ , of the flare in question this is an excellent approximation because the population of Fe XXVI is very small. As a result of the approximations we were left with three coupled linear differential equations in three unknowns. These were solvable by matrix methods without too much labor. The  $\alpha$ 's and  $Q$ 's were obtained from Jordan (1970).

Equations (5.1) were solved at each readout interval from 0304:50 on. At each time, the increase in emission measure from the previous readout was considered to be due to an increase in flare volume at constant density. All iron included in this increase was considered to be in a low ionization state and was deleted when computing the input to the next calculation. Thus if EM increased by 5%, the values of  $a_{22}$ ,  $a_{23}$ , and  $a_{24}$  obtained from the  $n$ th solution of equations (5.1) were multiplied by  $(1.05)^{-1}$  and used as initial conditions for the  $(n+1)$ th solution of the equations. The initial conditions at 0304:50 were set at  $a_{22} = .641$ ,  $a_{23} = .129$ , and  $a_{24} = .161$ . The electron density  $n_e$  was set at  $10^9$ , and  $A_{Fe} = 2 \times 10^{-5}$  and  $A_{He} = 0.2$  were used.

The results of the foregoing calculation are shown in Table IV.  $T_z$  is given as the temperature at which  $a_{24}(t)$  would obtain if the plasma were in a state of ionization equilibrium.  $\phi_L(T, T_z)$  is  $\phi_T$  from equation (4.8), and  $\phi_c$  is the continuum in the 0.174-0.190 band discussed in the previous sections. Thus  $\phi_L + \phi_c$  should be compared with the raw data  $\phi_G$ . This comparison is shown in figure 7. The agreement between the data and the calculation appears to be good except that the Goddard flux persists after the calculated curve has fallen off. The UCSD data were not available for this period, but it is likely that they would be unusable, since as  $T$  decreases the proportional counter data become unreliable.

Despite the apparent agreement between data and calculation in figure 7 the low density solution is probably not valid. From the rasters an upper limit on the flare area of about  $10^{20} \text{ cm}^2$  may be set. The ATM data for a large variety of flares suggest that the actual area is much smaller (Vorpahl et al., 1975; Kahler et al., 1975). With  $EM \approx 3 \times 10^{48} \text{ cm}^{-3}$ , we have  $n_e^2 h \geq 3 \times 10^{28}$ . Since flare heights,  $h$ , are typically  $\sim 10^9 \text{ cm}$  (Catalano and Van Allen, 1973),  $n_e^2 \geq 3 \times 10^{19}$  and  $n_e \geq 5 \times 10^9$ . The solution to equations (5.1) indicates that at such high densities,  $T_z$  is much nearer  $T$  than it is for  $n_e = 10^9$ . Therefore the high density case ( $T_z = T$ ) must be examined.

The high density case is easy to treat. One simply solves equation (4.8), assuming  $T = T_z$ . To determine the iron abundance, we calculate  $\phi_w$ , defined as  $\phi_T$  in equation (4.8) for  $A_{Fe} = 10^{-5}$ . We then make a least squares fit of the form  $m\phi_w = \phi_L$  where  $\phi_L$  is the measured line flux,  $\phi_G$  (measured) -  $\phi_c$ ; that is we minimize

Table IV

Time	$a_{24}(t)$	$T_z$ at $a_{24}(t)$	$\phi_L(T, T_z)$	$\phi_c$	$\phi_L + \phi_c$
0304:50	.161	13.8	2070	4805	6875
0305:57	.220	14.5	2710	4394	7104
0306:58	.268	15.1	3209	4120	7329
0308:00	.305	15.4	3410	3750	7160
0308:56	.306	15.4	3470	3525	6995
0309:57	.278	15.2	2948	3158	6106
0311:04	.289	15.3	2885	2553	5438
0312:06	.275	15.2	2569	2219	4788
0313:01	.265	15.1	2372	2073	4445
0314:09	.234	14.7	2046	1775	3821
0315:04	.247	14.9	2103	1778	3881
0316:11	.203	14.3	1597	1378	2975
0317:11	.195	14.2	1397	1233	2630
0318:08	.155	13.7	1027	1106	2133

REPRODUCIBILITY OF THE  
ORIGINAL PAGE IS POOR



$$s = \sum_i (m \phi_{wi} - \phi_{Li})^2 \quad (5.2)$$

Differentiating, we obtain

$$m = \frac{\sum_i \phi_{Li} \phi_{wi}}{\sum_i \phi_{wi}^2} \quad (5.3)$$

Assuming that the error in  $\phi_{Li}$  dominates we estimate the error,  $\delta m$ , as

$$\delta m = \left[ \sum_j \left( \frac{\partial m}{\partial \phi_{Lj}} \right)^2 (\delta \phi_{Lj})^2 \right]^{\frac{1}{2}} \quad (5.4)$$

or

$$\delta m = \frac{\left[ \sum_j \phi_{wj}^2 (\delta \phi_{Lj})^2 \right]^{\frac{1}{2}}}{\sum_j \phi_{wj}^2} \quad (5.5)$$

From equations (5.3) and (5.5) we obtain  $m = 1.11 \pm .14$ , for  $A_{He} = 0.2$ . For lower values of  $A_{He}$ ,  $m$  will be lower in inverse proportion to the assumed emission measure. The assumed emission measure is in turn inversely proportional to the curves in figure 6. Thus for  $A_{He} = 0.07$ ,  $m \approx 0.8$ . For  $A_{He} = 0.2$  we estimate  $A_{Fe} = 1.1 \times 10^{-5}$ . The data are displayed in Table V.

Figure 8 shows a plot of  $\phi_c + 1.11 \phi_w$  compared to the data,  $\phi_G$ . The point at  $t = 173$  was excluded from the calculation of  $m$  because of its great deviation from the points around it. As in the low density case the curve predicts less iron line flux than is observed late in the flare.

Table V

Time	$\phi_{wi}$	$\phi_{Gi}$	$\phi_{ci}$	$\phi_{Li}$
0301:45	2878	8394	3279	5100
(0302:53)	(3950)	(4214)	(4543)	(-329)
0303:48	4175	8994	4960	4034
0304:50	4230	8055	4805	3250
0305:57	3772	7555	4394	3161
0306:58	3427	8824	4120	4704
0308:00	2747	5417	3750	1667
0308:56	2532	4386	3525	861
0309:57	2061	7063	3158	3905
0311:04	1340	5907	2553	3354
0312:06	985	6472	2219	4253
0313:01	842	2496	2073	423
0314:09	541	5008	1775	3233
0315:04	606	4249	1778	2471
0316:11	308	2807	1378	1429
0317:13	250	4122	1233	2889
0318:08	187	3585	1106	2479
0319:10	126	1711	923	788

## 6. Discussion

In the previous section we arrived at an iron abundance of  $1.1 \times 10^{-5}$  for a helium abundance of  $2 \times 10^{-1}$  or an iron abundance of  $\sim 8 \times 10^{-6}$  in the limit of very low helium abundance. These values lie considerably below those found in other investigations. Walker et al. (1974a) recently determined an iron abundance  $2.6 \times 10^{-5}$  for a solar active region, based upon a detailed analysis of Fe XVII emission. Walker et al. (1974) had earlier placed the iron abundance at  $4 \times 10^{-5}$ , based upon a less complete model of the Fe XVII ion and lower quality observations than were used in the later paper. On the low side, Dupree (1972) set the iron abundance at  $2.0 \times 10^{-5}$  based on EUV observations.

Can our observations be reconciled with previous iron abundance estimates? To answer this question we must consider possible systematic errors and uncertainties in the calculation of the expected iron line flux. As we note in Section III, we have probably overestimated  $\alpha$ , the parameter relating the unresolved dielectronic recombination satellite line flux to the resonance line flux. If so, the expected line flux for a given  $A_{Fe}$  is overestimated by a factor of about 1.1. We noted in Section IV that the continuum subtraction might result in an error as large as 20% in the line flux. Thirdly a systematic error in the temperature estimate in the early phase of the flare could result in an error in the expected flux. For example, an overestimate of T by  $2 \times 10^6$  K at a true temperature of  $2 \times 10^7$  K results in an underestimate of EM by 17% and an overestimate of the expected line flux per unit EM by 51%, for a net overestimate of the expected flux by 29%. Since the high counting rates are heavily weighted, a temperature error here would be most effective. Errors larger than that discussed above are improbable. If all of the above factors are considered, the result for  $A_{He} = 0.2$  becomes  $(1.1 \pm .14) \times (1.1) \times (1.2) \times (1.29) = 1.9 \pm .24$ .

Two other factors are not as easy to estimate. Sufficient high quality iron line spectra are not available to verify theoretical line strength calculations. The factor, G, is based upon measurements of low Z ions. Parkinson (1972), however, from an excellent magnesium spectrum, found  $G = 1.04$ , in good agreement the oxygen measurements of Rugge and Walker (1971) and with our assumed value of 1.1. The satellite line intensities have not been verified, either. Finally, we

should consider the consequences of a breakdown of the assumption that the flare plasma is isothermal. Because the continuum flux increases more than in proportion to the temperature, if the plasma contains components at temperatures greater than  $T$  (as it must if the plasma is not isothermal), the emission measure based upon an isothermal plasma will be an overestimate. However, the line flux increases more rapidly with  $T$  (around  $2 \times 10^7$  K) than does the continuum. Then the line to continuum ratio will be higher than that for an isothermal plasma. Thus a breakdown in the isothermality assumption would result in an overestimate of the iron abundance.

Taking into account the discussion of the preceding paragraphs, it appears that our  $A_{Fe}$  may be reconciled with other low estimates but not with values much in excess of  $2 \times 10^{-5}$ . Further, the helium abundance must be high for this reconciliation. This experiment thus lends support to a helium abundance relative to hydrogen around 0.2. The measurement is not good enough to make a definitive determination of  $A_{He}$  relative to  $A_{Fe}$ .

The determination of the solar helium abundance is an important unsolved problem. The continuum emission processes are well enough understood that the helium abundance is the major unknown in calculating continuum emission in some wavelength and temperature regimes (see Culhane, 1969). We have chosen to attack the problem by measuring the line to continuum ratio for helium-like iron during a solar flare, in the hope that a definitive iron abundance measurement, coupled with our observations, would allow the helium abundance to be determined. This approach has the disadvantage that iron line emission is not well understood and that solar flare conditions impose analysis difficulties. However, flare observations have the advantage that substantial continuum emission occurs in a short wavelength region that is line free. A large number of high quality solar flare iron line spectra need to be analyzed to verify the iron line emission theory and the iron abundance before the technique used here can yield a helium abundance determination. Crystal spectrometer or Ross filter measurements, together with high quality continuum spectra, perhaps measured with a cooled solid state detector, can then provide a good determination of the solar helium abundance.

## FIGURES

- Figure 1 The mass absorption coefficients of iron and manganese.
- Figure 2 The calculated response of the UCSD proportional counter to thermal continuum spectra. The effective channel edges reflect a 6% gain decrease in this plot.
- Figure 3 The UCSD detector response at a total counting rate of  $2 \times 10^4 \text{ sec}^{-1}$ ,  $1 \times 10^3 \text{ sec}^{-1}$  of which are iron line counts. A 5% gain decrease and an additional 5% decrease due to high counting rates are assumed.
- Figure 4 The temperature dependent multiplying factors for inner-shell excitation and dielectronic recombination satellite lines. Data are from calculations by Bhalla et al. (1975).
- Figure 5 The Goddard 0.174 - 0.190 nm x-ray flux as a function of time and the linear least squares fit to the data. One  $\pm 1\sigma$  error bar is shown.
- Figure 6 The continuum at 0.2 nm as a function of electron temperature with the helium abundance,  $A_2$ , as a parameter. The flux is normalized such that the flux for  $A_2 = 0.07$  is unity at each temperature.
- Figure 7 Comparison of  $\Phi_L + \Phi_C$  calculated assuming density =  $10^9 \text{ cm}^{-3}$  with the measured 0.174 - 0.190 nm flux.
- Figure 8 Comparison of  $\Phi_C + 1.11 \Phi_w$  and  $\Phi_G$  for the case  $T = T_z$ . The helium abundance is assumed to be 0.2, relative to hydrogen.

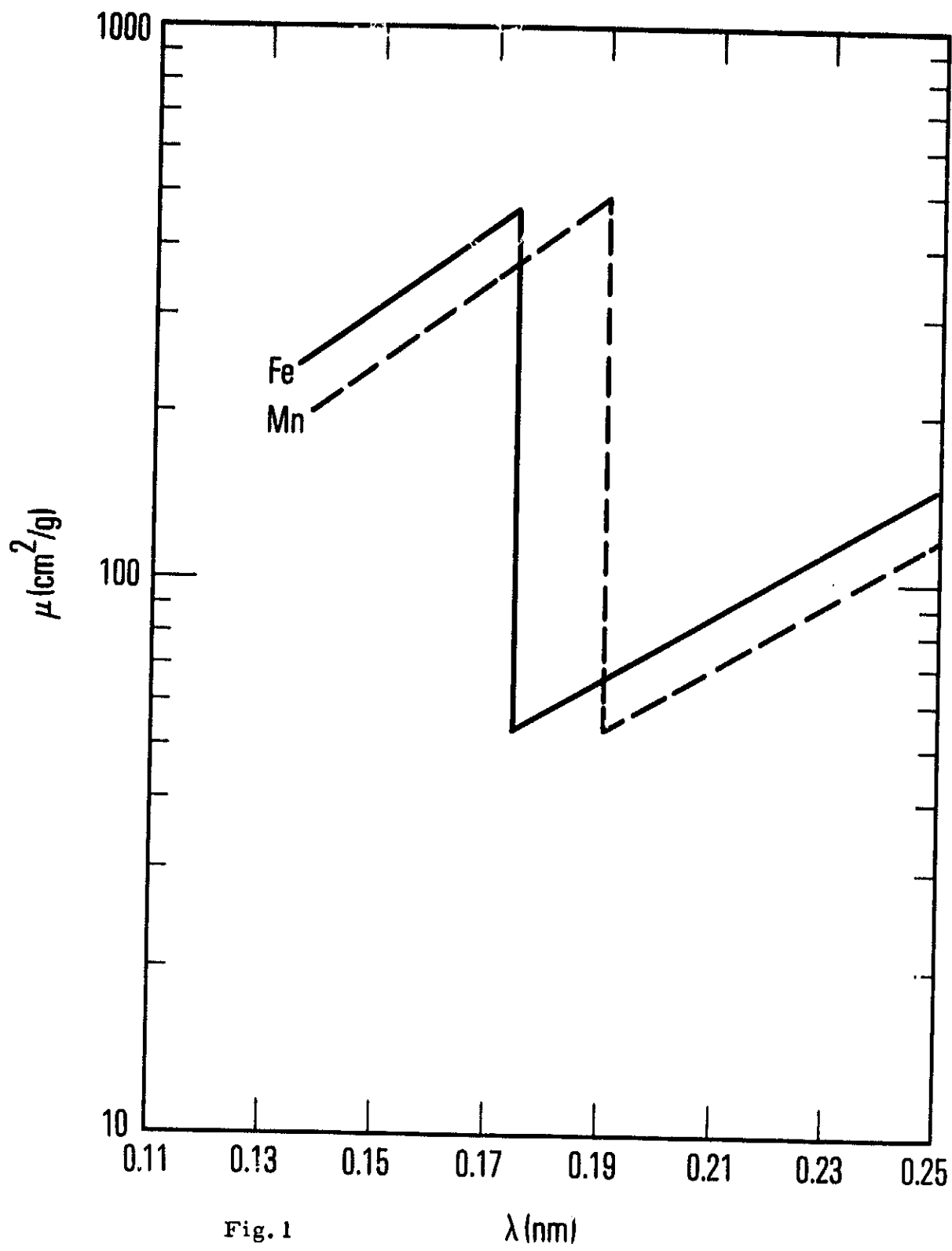


Fig. 1

$\lambda$  (nm)

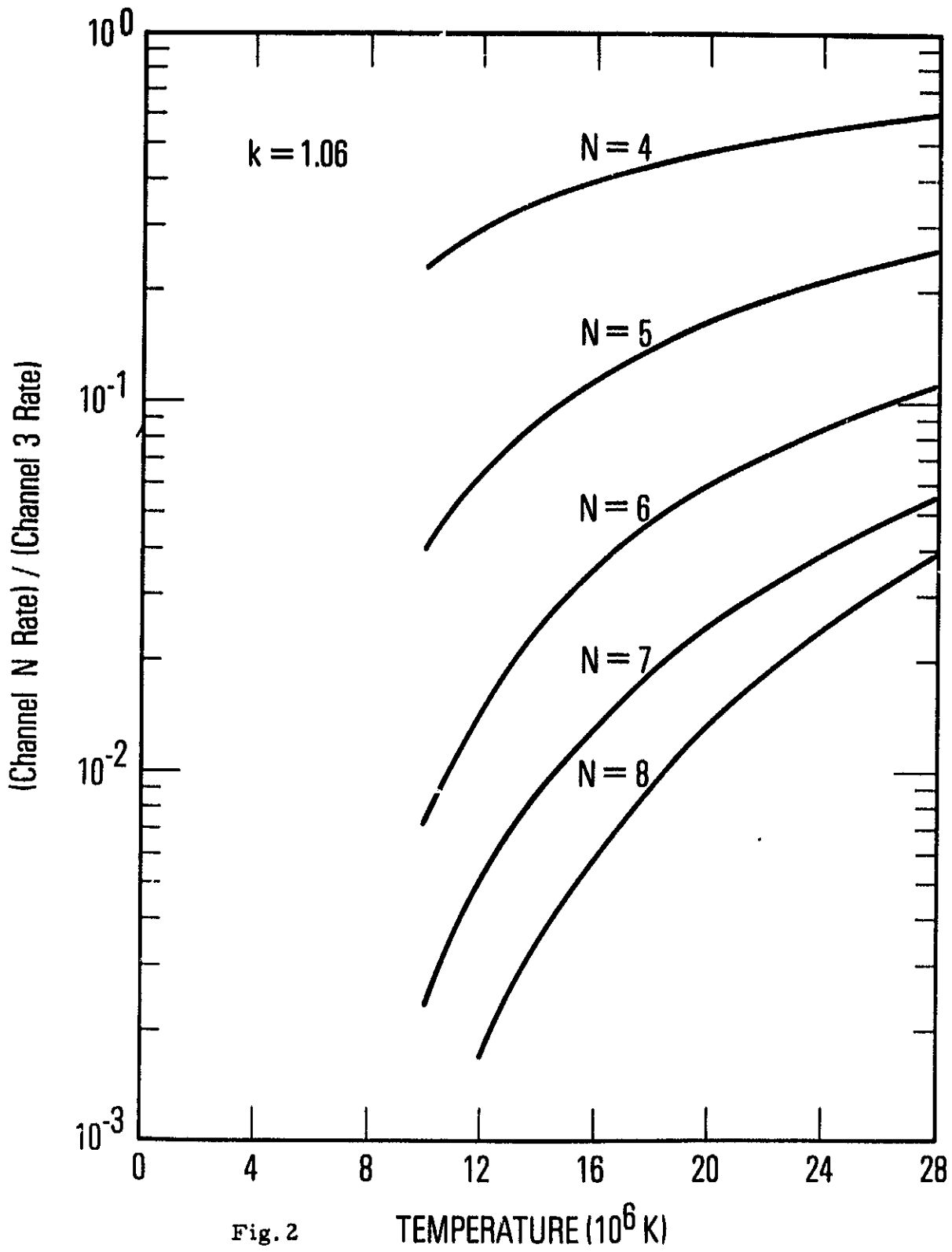


Fig. 2

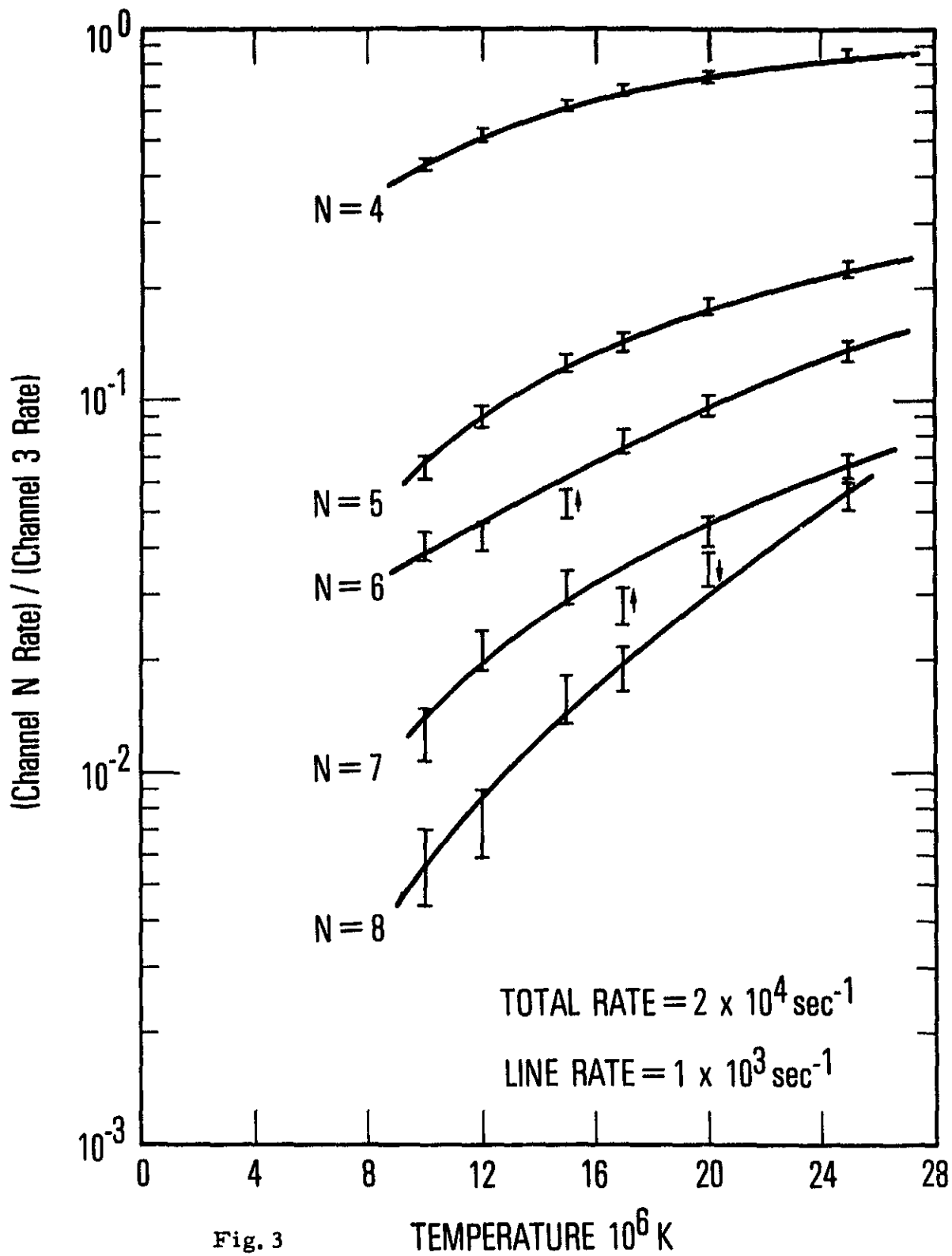


Fig. 3



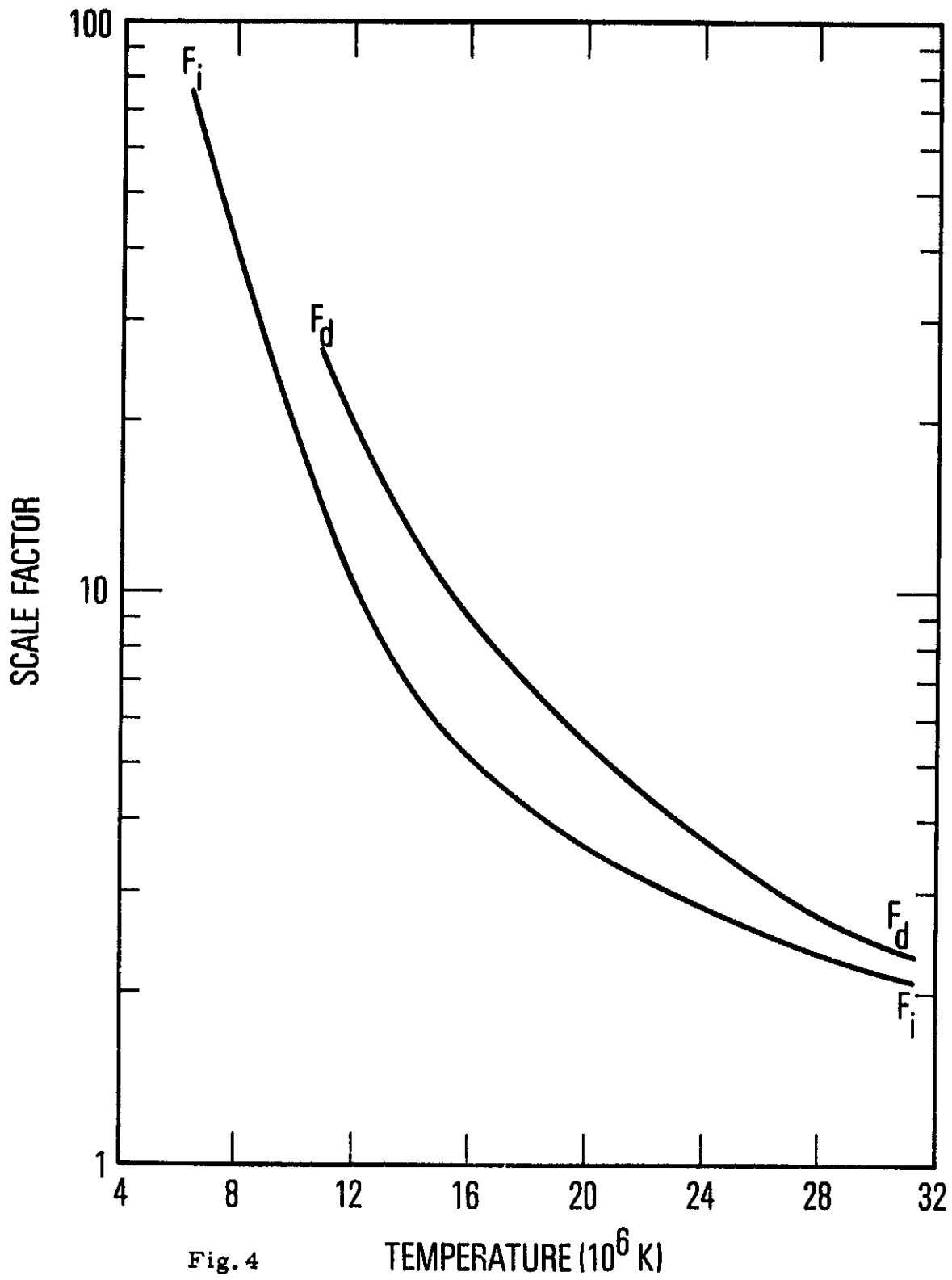


Fig. 4

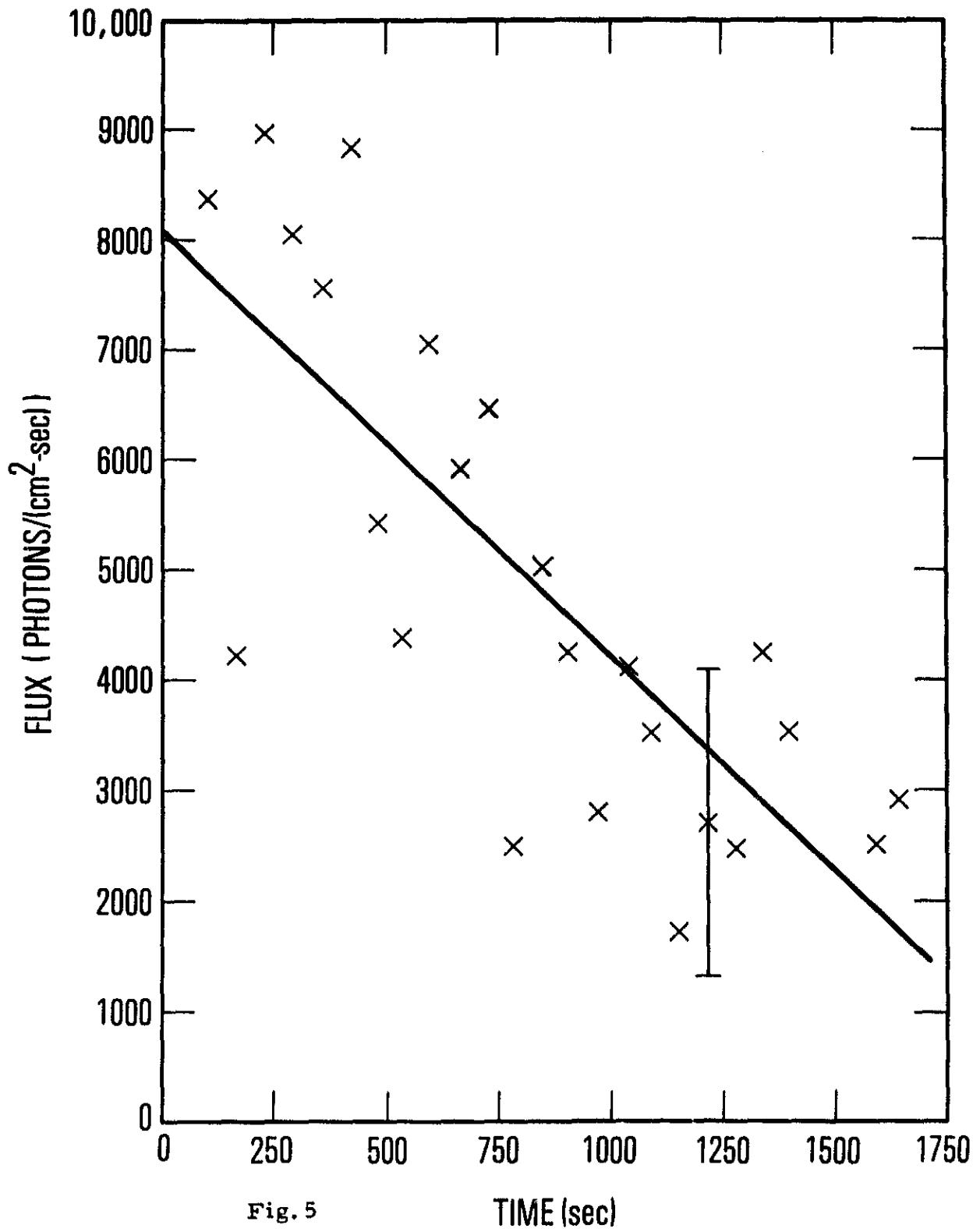
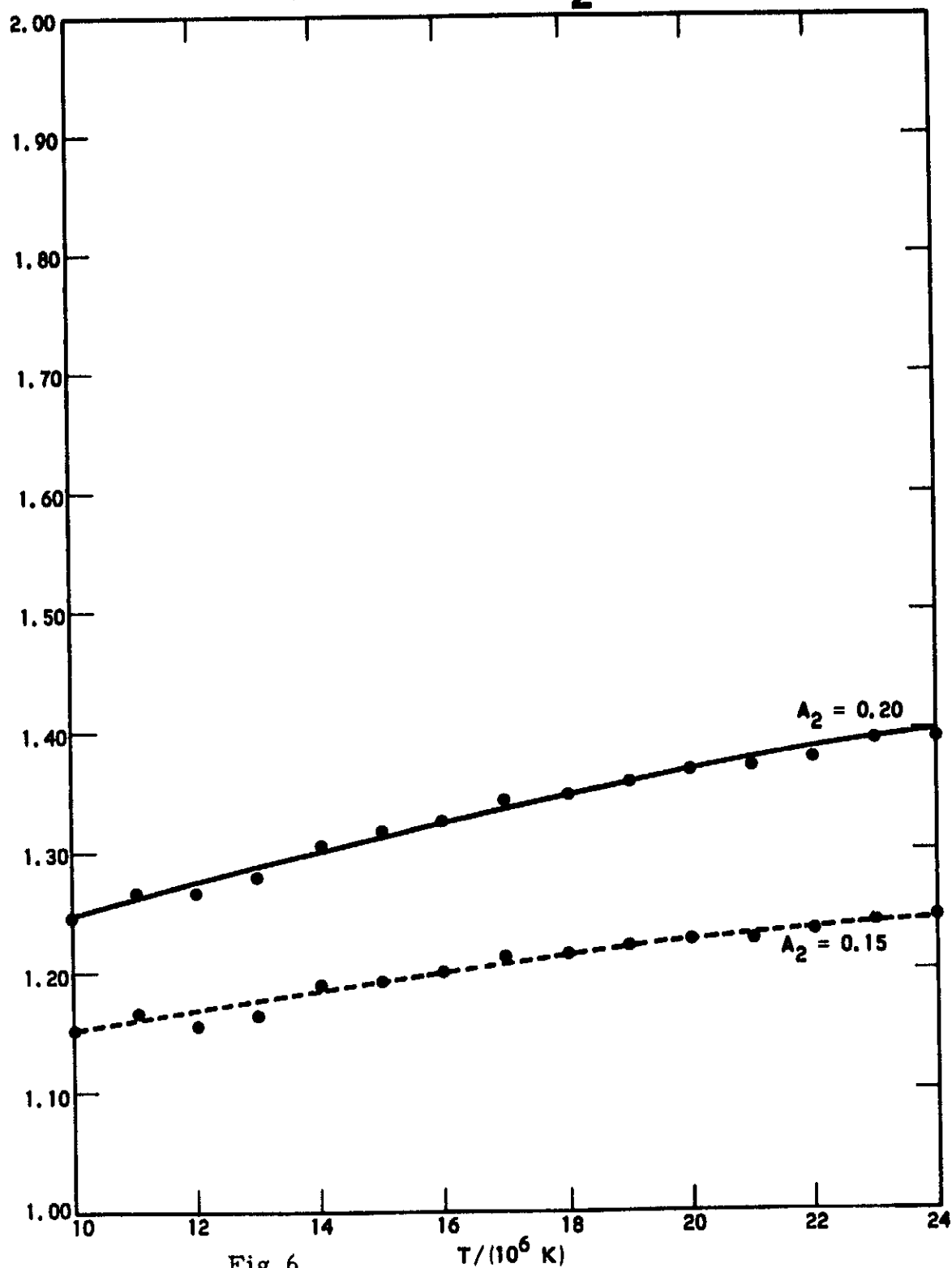


Fig. 5

(Continuum at  $\lambda = 0.2 \text{ nm}$ )/(Continuum at  
 $\lambda = 0.2 \text{ nm}$  for  $A_2 = 0.07$ )



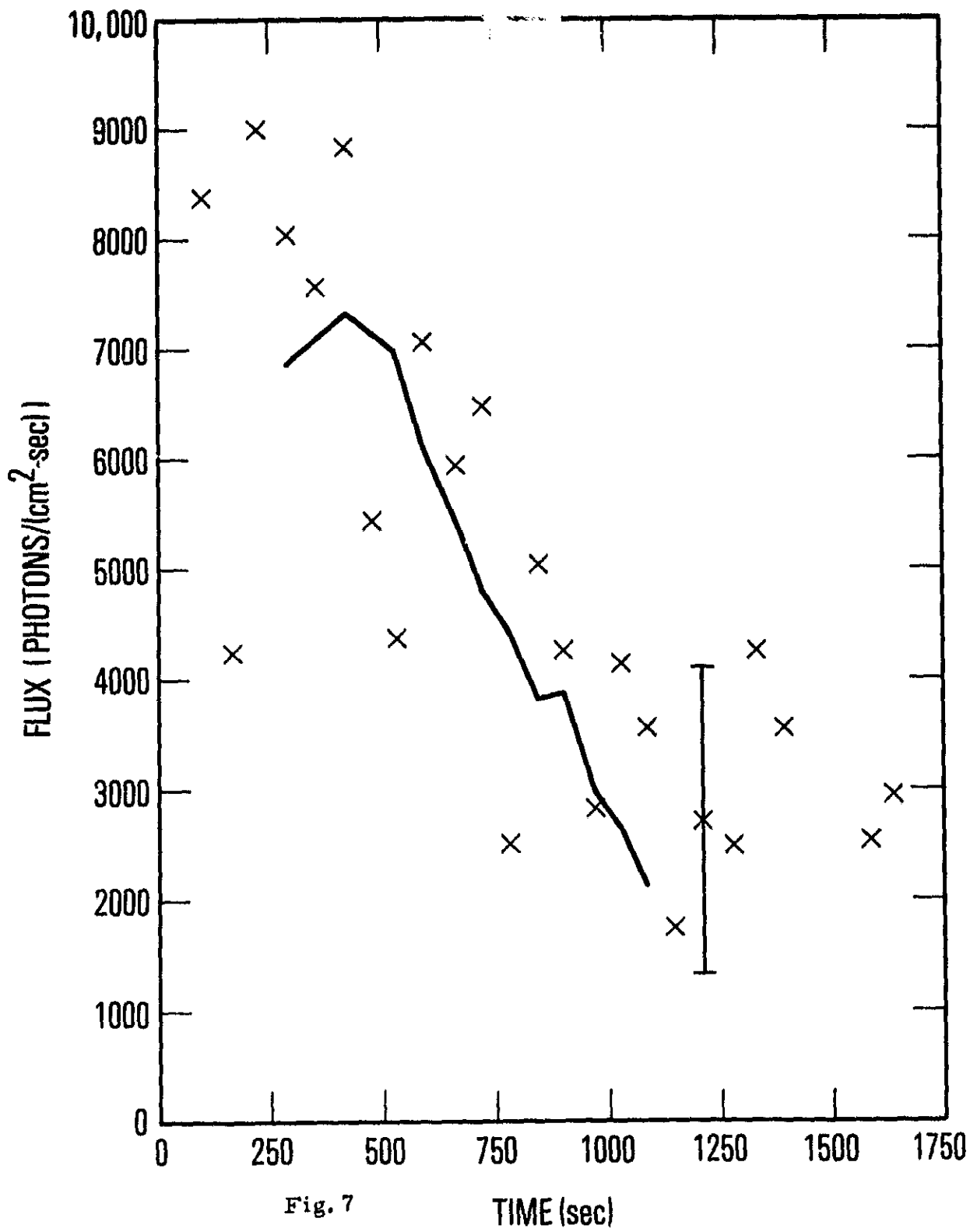


Fig. 7

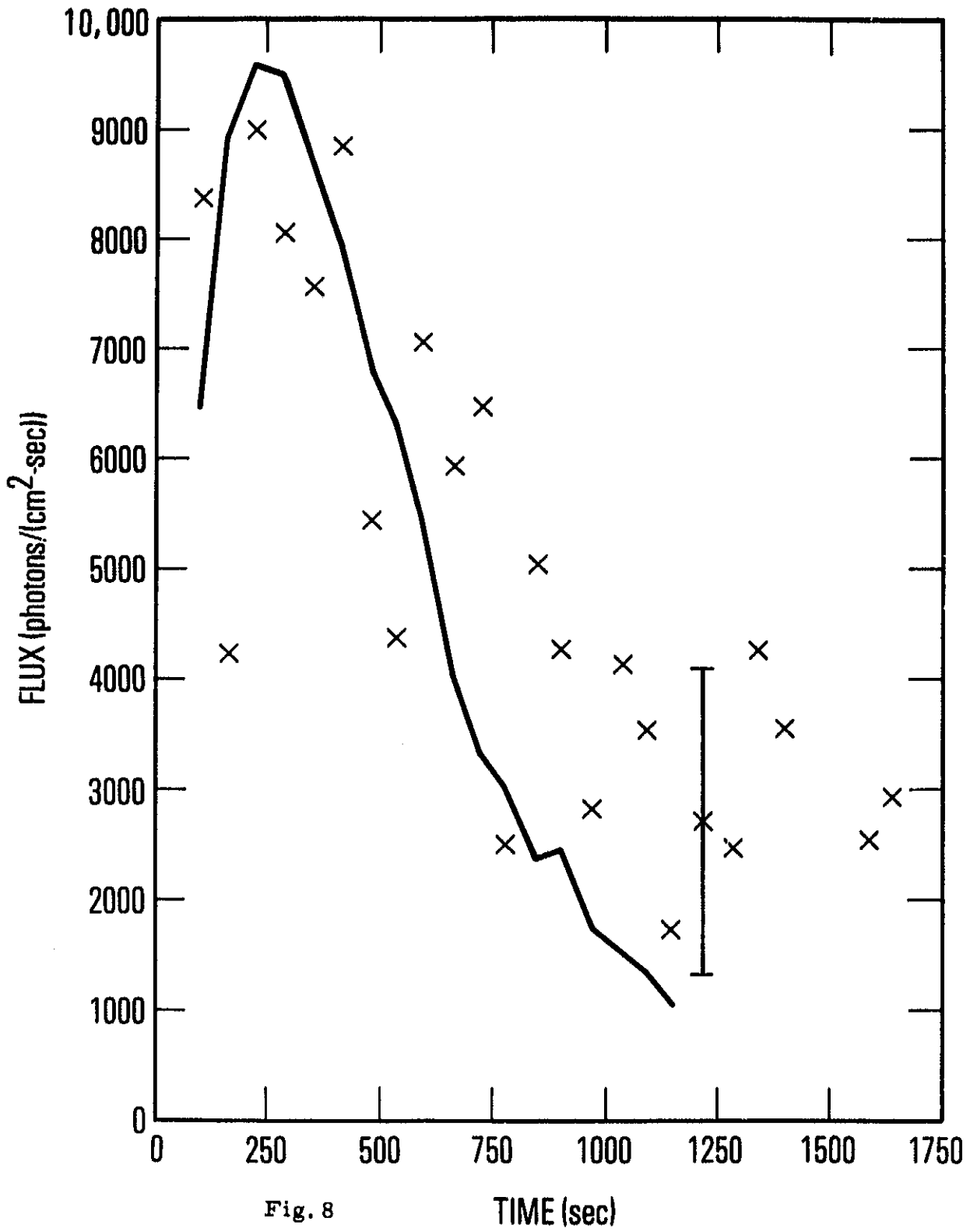


Fig. 8

## REFERENCES

- Bhalla, C. P., Gabriel, A. H., and Presnyakov, L. P.: 1975, "Dielectronic Satellite Spectra for Highly-Charged Helium-like Ions II-Improved Calculations," Mon. Not. R. Astro. Soc. (to be published).
- Blumenthal, G. R., Drake, G. W. F., and Tucker, W. H.: 1972, Ap. J. 175, 205.
- Catalano, C. P., and Van Allen, J. A.: 1973, Ap. J. 185, 335.
- Cox, D., and Tucker, W.: 1969, Ap. J. 157, 1157.
- Culhane, J. L., Sanford, P. W., Willmore, A. P., Blades, J., and Nettleship, R.: 1967, I.E.E.E. Trans. Nuc. Sci. NS-14, 38.
- Culhane, J. L.: 1969, Mon. Not. R. Astro. Soc. 144, 375.
- Dupree, A. K.: 1972, Ap. J. 178, 527.
- Gabriel, A. H., and Jordan, C.: 1969, Mon. Not. R. Astro. Soc. 145, 241.
- Gabriel, A. H.: 1972, Mon. Not. R. Astr. Soc. 160, 99.
- Gabriel, A. H., and Jordan, C.: 1973, Ap. J. 186, 327.
- Jordan, C.: 1970, Mon. Not. R. Astro. Soc. 148, 17.
- Kafatos, M. C., and Tucker, W. H.: 1972, Ap. J. 175, 837.
- Kahler, S. W., Krieger, A. S., and Vaiana, G. S.: 1975, "Morphological Evolution of X-ray Flare Structures from the Rise through the Decay Phase," ASE-3668 (to be published).
- McKenzie, D. L., Datlowe, D. W., and Peterson, L. E.: 1973, Solar Physics 28, 175.
- Neupert, W. M., Gates, W., Swartz, M., and Young, R.: 1967, Ap. J. (Letters) 149, L79.
- Parkinson, J. H.: 1972, Nature Phys. Sci 239, 68.

- Rugge, H. R., and Walker, A. B. C., Jr.: 1971, Solar Physics 18, 244.
- Shore, B. W.: 1969, Ap. J. 158, 1205.
- Sterk, A. A., Kieser, F., Peck, S., and Knox, E.: 1972, "EUV and X-ray Spectroheliograph for OSO-H," General Electric Report #DIN 71SD4268.
- Vorpahl, J. A., Gibson, E. G., Landecker, P. B., McKenzie, D. L., and Underwood, J. H.: 1975, "Observations of the Structure and Evolution of Flares with a Soft X-ray Telescope" (in preparation).
- Walker, A. B. C., Jr.: 1972, Space Sci. Revs 13, 672.
- Walker, A. B. C., Jr., Rugge, H. R., and Weiss, K.: 1974, Ap. J. 192, 169.
- Walker, A. B. C., Jr., Rugge, H. R., and Weiss, K.: 1974a, Ap. J. 194, 471.